Engineered Science

RESEARCH PAPER

View Article Online

Electrophoretic Deposition and Thermo-Chemical Properties of Al/Fe_2O_3 Nanothermite Thick Films

Jie Wu,[1,2] Songbai Xue,[1*] Denzel Bridges,[2] Yongchao Yu,[2] Cary Smith,[2] Kunlun Hong,[3] Curtis Hill,[4] Zhili Zhang,[2] Zhili Feng[5] and Anming Hu[2*]

We have successfully fabricated α-Fe_2O_3 oxidizers with different shapes, including nanoparticles (NPs, diameter: ~22.1 nm), nanorods (NRs, length: 385.3 nm) and nanowires (NWs). For the Al/Fe_2O_3 NPs thermite reaction, as the nominal weight ratio for Al/Fe_2O_3 (NPs) reaches 2.5:1, the fastest combustion velocity (2.03 m/s), the largest instant plume propagation speed (10.71 m/s) as well as the maximum heat release (~9.46 kJ/g) can be achieved. However, with the same nominal weight ratio, the average combustion velocity and the instant plume speed of Al/Fe_2O_3 (NRs) and Al/Fe nitrilotriacetic acid precusors NWs (FeNTA,) nanothermite are only about 0.16 m/s and 4.96 m/s, and 0.098 m/s and 3.28 m/s, respectively. This is probably due to the shape difference that renders different contact configurations between nano-fuel and nano-oxidizer. In addition, an incomplete calcination of FeNTA is also responsible for such a low combustion velocity. The reaction products were further identified by SEM and XRD analysis. Accordingly, the reaction mechanisms for the examined nanothermites were mainly controlled by the oxygen transfer dynamics.

Keywords: Nanothermite; Electrophoretic deposition (EPD); Nanostructure; Reaction products

Received 28 June 2018**, Accepted** 12 August 2018

DOI: 10.30919/es8d751

1. Introduction

Nano-thermite, one kind of nano-energetic materials, is known to consist of a fuel and an oxidizer, one of which is in the nano-scale. Compared to micro-sized thermite composite, nano-thermite has the advantages of a larger energetic density, a lower triggering temperature, a higher combustion velocity, and most importantly, a greater amount of heat release.[1-3] These advantages are mainly attributed to their nano-scale characteristic that contributes to a more intimate interface contact between nano-fuel and nano-oxidizer, i.e. a mass diffusion length.[4,5] Hence, nano-thermite has extensive potential for applications of nano-scaled welding,[6] ignition devices,[7] as well as power and heat generation.[8,9]

There are increasing interests in improving the combustion performance of a variety of nanothermite systems.[3] In principle, the factors influencing combustion include the selection of materials and their stoichiometry,[10] mixture density,[11] particle size, and crucially, the quality of mixing state of fuel and oxidizer.[12] With the aim of maximizing the interface contact in a uniform mixing, considerable efforts have been put into assembling composite mixtures, such as using electrostatic assembly,[13] magnetron sputtering,[14] ligand coating[15] and sol-gel methods.[16] The latter two methods are facile and effective to enhance the reactivity. However, significant amounts of organics are introduced, in turn offsetting the advantages of organization. Recently, it has been reported that electrophoretic deposition (EPD) is a convenient and low-cost method to prepare nanothermite film with the advantages of a controlled thickness and some complex morphology.[12] Both Sullivan et al.[12] and Zhang et al.[2] have successfully deposited the micro-scaled Al/nano-CuO and nano-Al/nano-Fe_2O_3 thermites onto a Cu electrode, respectively. Both nanothermites displayed superior combustion performance. This is attributed to the retained nano-scale particle shape with uniform mixing in deposited films. So, in this study, EPD is employed to prepare the examined nanothermites.

Another popular method to tailor the combustion performance of nanothermite is to control both the morphology and the size of nano-fuel or oxidizer since they can influence the mass transmission and the interface contact area.[17] Recently, various metal-oxide nanostructures (e.g., nanowires (NWs),[18] nanorods (NRs),[19] nanofibers,[20] nanospheres[21]) have been successfully fabricated and implemented in developing nanothermites with superior combustion performance. A recent study on Al/CuO nanothermite reaction showed that the pressurization rate from a composite of Al (NPs)/CuO (NWs) was about ten times larger than those from the Al/CuO nanothermite in micro-scale.[22] Other methods like

---

[1] *College of Materials Science and Technology, Nanjing University of Aeronautics and Astronautics, Nanjing 210016, People's Republic of China*
[2] *Department of Mechanical, Aerospace and Biomedical Engineering, University of Tennessee Knoxville, 1512 Middle Drive, Knoxville, TN 37996, USA*
[3] *Center of Nanophase Material Sciences, Oak Ridge National Laboratory, Oak Ridge, TN 37830, USA*
[4] *CK Technologies, 268 Lewis Tate Rd. Meridianville, AL 35759, USA*
[5] *Materials Science and Engineering Division, Oak Ridge National Laboratory, Oak Ridge, Tennessee 37831, USA*
E-mail:xuesb@nuaa.edu.cn ; ahu3@utk.edu*

fabricating the core-shell nanostructures[17,23] and 3D ordered porous structured Fe_2O_3/Al Nanothermite[24] have also been developed to optimize energetic properties of nanothermite. These nanostructure modifications of thermites have improved their energy performance through changing the interface contact distance and area.

In this study, we have fabricated α-Fe_2O_3 oxidizers with different shapes, including sphere-like, rod-like and wire-like. Afterwards, Al/Fe_2O_3 (NPs) nanothermite with different nominal weight ratios were prepared through EPD method to explore the optimized ratio for the fastest nanothermite reaction. Under the optimal ratio, another two kinds of Al/Fe_2O_3 (NRs) and Al/FeNTA (NWs) nanothermite were prepared as well. Then, comparative studies on the shape effect of α-Fe_2O_3 nanomaterials on the combustion performance of nanothermite were conducted. The relevant oxygen transfer dynamics was also discussed to explain the difference. Finally, the reaction mechanisms of nanothermites were also qualitatively determined through the identification of reaction products.

2. Experimental

2.1 Fabrication of Nano-thermites

Al nanoparticles (NPs) used in this research was commercial available with the average particle size in a range of 60-70 nm.[25] Nano-scaled Fe_2O_3 oxidizers with three kinds of shapes (sphere,[26] rod,[27] and wire[28]) were fabricated based on the previous reports. In brief, to obtain Fe_2O_3 NPs, a mixture of 40 mL of 0.3M $Fe(NO_3)_3$ and 1.5M urea aqueous solution was prepared first and then this slurry mixture was sealed in a Teflon-lined stainless-steel for hydrothermal reaction for 12 hours. Fe_2O_3 NRs were also synthesized via a hydrothermal method (16 hours) through mixing aqueous $FeCl_3$ solution (0.86 M) and 1, 2-propanediamine together (volume ratio: 1:1). For Fe_2O_3 NWs, 0.15M $FeCl_3$ aqueous solution was first mixed with isopropanol. Nitrilotriacetic acid (NTA) was added then. Chelating compounds ($(\text{-Fe-NTA-})_n$) were subsequently obtained also through hydrothermal method for 24 hours. However, the following heat-treated process converting $(\text{-Fe-NTA-})_n$ to α-Fe_2O_3 lead to the decrease in the length of NW, from several microns to 1-2 microns. In order to maintain the nanowire length, chelating compounds, instead of Fe_2O_3 NWs, was used in producing nanothermite with Al NPs.

2.2 Preparation of Al/Fe_2O_3 nanothermite by EPD method

An EPD method was used to prepare Al/Fe_2O_3 nano-thermite films. Before deposition, Cu sheets serving as the cathode are polished and ultrasonically cleaned with ethanol first. Afterwards, a carbon electrode accompanied with the clean Cu sheet are inserted vertically into the electrolyte with a constant distance of ~1.0 cm. The electrolyte contains ethanol and acetylacetone (volume ratio of 1:1) with sodium dodecyl sulfate (SDS, 0.0025 M) as additive.[12] Al NPs and Fe_2O_3 NPs with different weight ratios were dispersed into the electrolyte (Table 1) to explore the most appropriate weight ratio for enhancing the combustion performance. Under this satisfactory ratio, EPD samples of Al/Fe_2O_3(NRs) and Al/FeNTA(NWs) were prepared for comparison. Fig. 1 presents the partial optical images of EPD samples of Al/Fe_2O_3 (NPs), Al/Fe_2O_3 (NRs) and Al/Fe_2O_3 (NWs). For each EPD cell, the total volume of solvent is fixed at 20 mL and the concentration is controlled at 2 g L^{-1} in the given dispersant. The applied voltage, current and deposition time were 100V, 0.05A and 20 min, respectively. Herein a parameter of equivalence ratio Φ is introduced, which represents the ratio between actual fuel/oxidizer dispersed in the electrolyte and the fuel/oxidizer ratio in a stoichiometric reaction, shown as follows

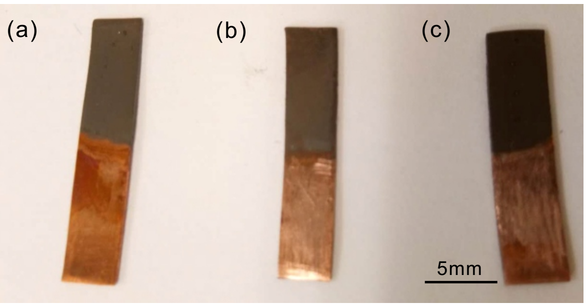

Fig. 1 Optical micrograph of EPD sample of Al/Fe_2O_3 (NPs), Al/Fe_2O_3 (NRs) and Al/Fe_2O_3 (NWs) nanothermite.

$$\Phi = {}^{(F/O)_{solution}}\!\Big/_{(F/O)_{stoich}} \tag{1}$$

where "F" means fuel; "O" means the oxidizer. The stoichiometric ratio of fuel to oxidizer was 2:1, according to the following equation:

$$2Al + Fe_2O_3 \rightarrow Al_2O_3 + 2Fe \tag{2}$$

Note that the calculations are done on a molar basis.

2.3 Characterization

The microstructure observation of the nano-thermite was conducted with a Zeiss 147 Auriga Scanning Electron Microscope (SEM). For the Particle size statistics of Fe_2O_3 NPs, about 235 points were selected for the statistical analysis and the average value was taken as the final result. In addition, for the length statistics for Fe_2O_3 NRs, about 224 points have been selected to calculate the average value. Energy Dispersive X-ray Spectroscopy (EDX) measurements were performed using a Zeiss MA15 EVO SEM equipped with a Bruker xFlash 6|30 detector. X-ray diffraction (XRD) measurements of samples were examined on a Panalytical Empyrean X-ray Diffractometer (λ = 0.15406 nm). Differential scanning calorimetry (DSC) and Thermogravimeter (TGA) analysis was performed using a Netzsch-Gerätebau STA 449 C Jupiter Thermo-microbalance in N_2. The heating rate is adjusted to be 10 °C/min when TGA-DSC is conducted. The ultraviol-tevisible spectroscopy (UV-vis) of nano-Fe_2O_3 oxidizers was also measured. Thermite films deposited on Cu substrate were triggered in one corner using a nanosecond laser beam. The high-speed video of the combustion process was recorded by a Power View HS-650 high-speed camera (1500 frames/second).

3. Results and Discussion

3.1 Morphology and characterization of nano-Fe_2O_3 oxidizers

Fig. 2 shows the SEM images of Al NPs, Fe_2O_3 NPs, Fe_2O_3 NRs and FeNTA NWs, and corresponding characterizations. Al NPs are spherical in nature but with high aggregation Fig. 2a. The average particle size of Al NPs is in a range of 60-70 nm. Also, Fe_2O_3 NPs are almost spherical in shape and with a smaller size than Al NPs Fig. 2b. The statistic particle diameter distribution Fig. 2f reveals the average diameter of Fe_2O_3 NPs is around 22.1 nm. For Fe_2O_3 NRs Fig. 2c, a typical rod-like morphology is observed. The average length is around 385.3 nm Fig. 2g and the diameter ranges from 65 to 75 nm. Fig. 2d shows a low magnified SEM image of FeNTA NWs. Clearly, all of them display a wire-shaped nanostructure with a

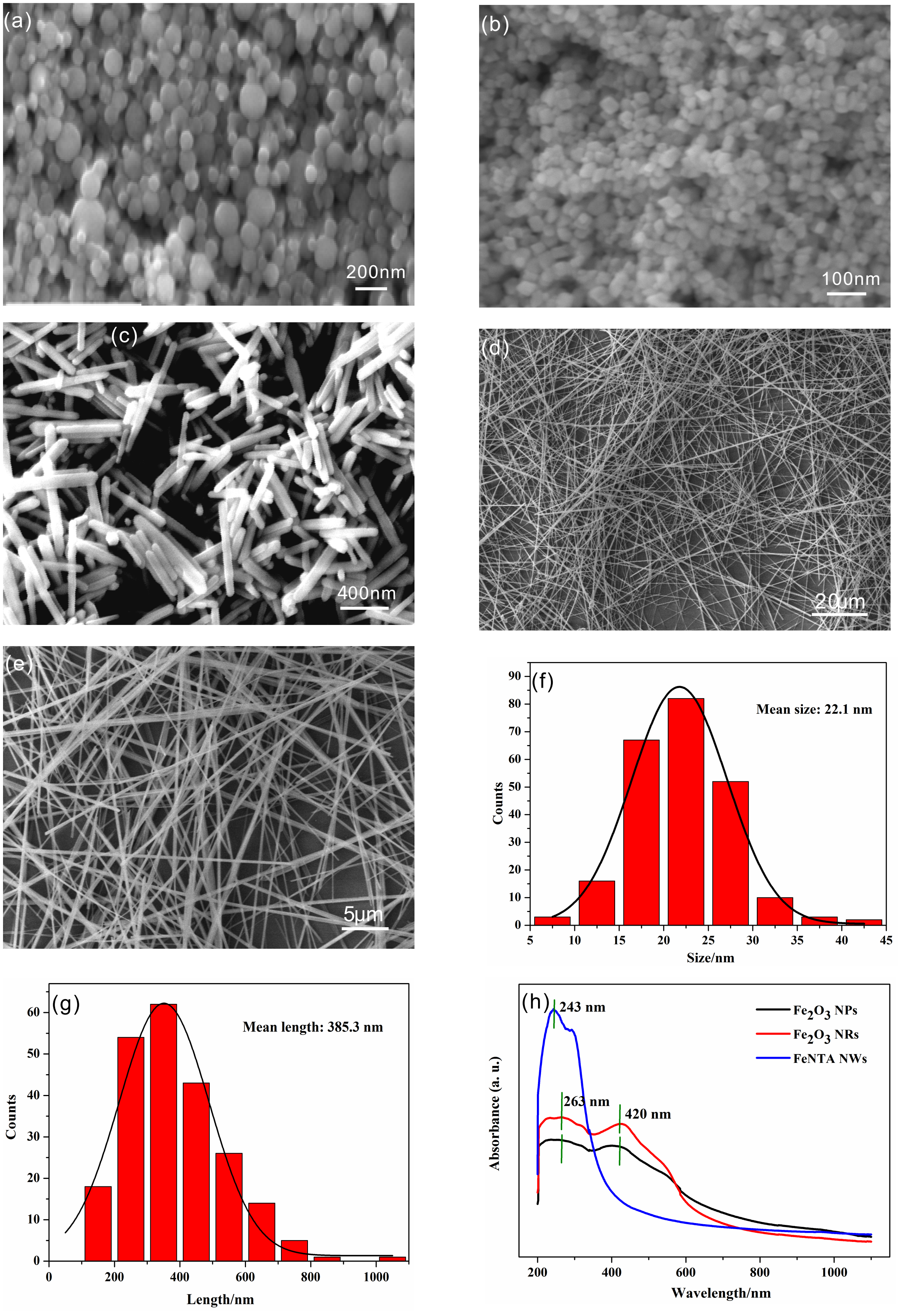

Fig. 2 (a) SEM image of commercially-available Al NPs (Diameter: 60-70 nm); (b) SEM image of Fe_2O_3 NPs; (c) SEM image of Fe_2O_3 NRs; (d) SEM image of FeNTA precursor NWs; (e) Magnified SEM image of NTA precursor NWs; (f) Particle size statistics for Fe_2O_3 NPs; (g) Length statistics for Fe_2O_3 NRs; (h) UV-vis spectra of Fe_2O_3 NPs, Fe_2O_3 NRs and FeNTA NWs.

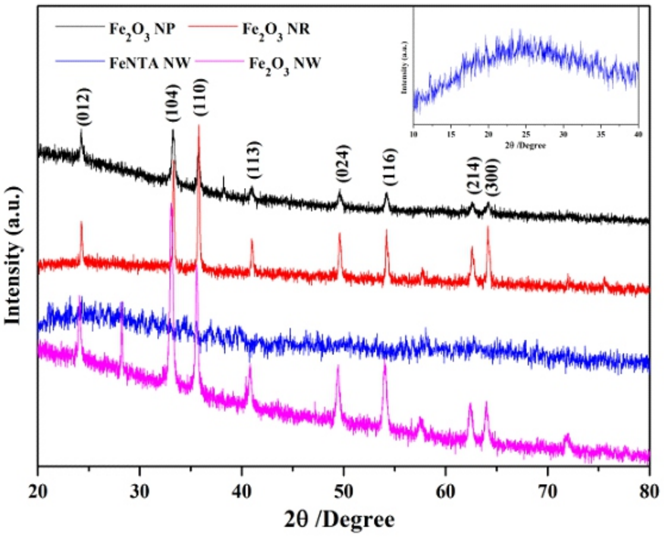

Fig. 3 XRD analysis of three kinds of nano-Fe_2O_3 oxidizers.

length of several tens of micrometers. Fig. 2e exhibits the magnified image of FeNTA NWs, showing a smooth surface. Fig. 2h gives the UV-vis spectrums of Fe_2O_3 NPs, Fe_2O_3 NRs and FeNTA NWs. It is obvious that the UV-vis spectra of Fe_2O_3 NPs and Fe_2O_3 NRs display a similar absorbance in both ranges of near-infrared and visible light. Both of their surface plasmon resonance (SPR) peaks emerge at ~263 nm and ~420 nm. For FeNTA NWs, the strong absorbance only occurs at ~243 nm. Also, the optical gaps of *α*-Fe_2O_3 NPs and NRs are around 1.38 ev, while that of *α*-FeNTA NWsnanowires is around 2.92 ev. This distinct difference is probably attributed to the crystalline phase difference. Fig. 3 presents XRD analysis results of three kinds of nano-Fe_2O_3 oxidizers. For Fe_2O_3 NPs and NRs, the positions of their representative diffraction patterns are similar, which are well indexed to the standard hematite (α-Fe_2O_3) with a rhombohedral structure (JCPDS: 33-0664). In addition, in Scherrer equation ($\tau = 0.9\lambda/(\beta \cos \theta)$), a larger FWHM indicates a smaller grain size. Since the XRD of α-Fe_2O_3 NPs have larger FWHM, they should have finer crystalline size than α-Fe_2O_3 NRs. In addition, it is obvious that FeNTA precursor NWs display an amorphous nature without any characteristic diffraction peaks present. A typical swelling shape around 20° is inserted in the XRD graphs. To verify a full converting of Fe_2O_3 precursor NWs to Fe_2O_3 NWs after calcination, Fe_2O_3 precursor NWs calcined at 500℃for 24 hours were taken for XRD analysis, the result of which is shown in Fig. 3. It is clear that all the diffraction peaks for the calcinate of Fe_2O_3 precursor NWs are matched well with the standard α-Fe_2O_3 (JCPDS: 33-0664).

3.2 Morphology and characterization of EPD films

To explore the combustion velocity of Al/Fe_2O_3 (NPs) nanothermite as a function of their equivalence ratio (Φ), Al NPs and Fe_2O_3 NPs with different weight ratios are dispersed in the electrolyte solution, as listed in Table 1. The ignition of these nanothermite with laser triggering was also shown in Table 1. As can be seen, Al/Fe_2O_3 (NPs) nanothermite reaction with Φ value ranging from 1.48 to 10.37 can be self-propagated, locally or fully, while nanothermites with Φ value of 0.74, 0.99 and 11.85 can not display a self-sustained combustion. Fig. 4 presents the corresponding combustion velocity and the instant plume speed of nanothermite as a function of Φ value. Clearly, with Φ value increasing from 2.96 to 7.41, both the combustion velocity

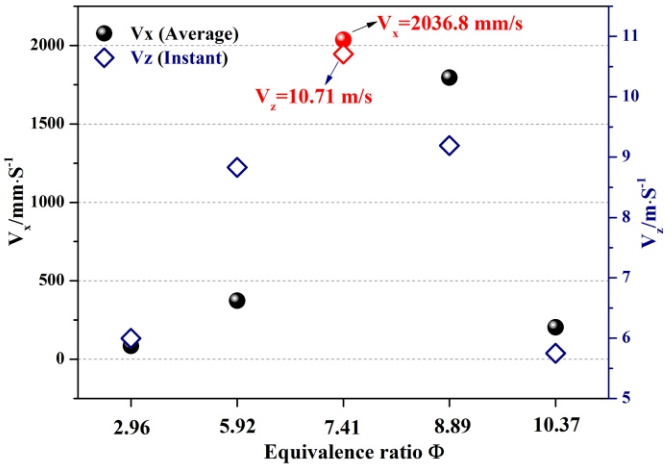

Fig. 4 The dependence of combustion velocity ($V_{x(Average)}$; $V_{z(Instant)}$) with the equivalence ratio Φ.

Table 1. Weight of Al and Fe_2O_3 nano-materials in the electrolyte and their combustion situation.

Weight ratio (Al: Fe_2O_3)	Nominal equivalence ratio Φ	Practical Weight (Al: Fe_2O_3)/mg	Trigger situation
1: 4	0.74	8; 32	Non Self-propagation (NSP)
1: 3	0.99	10; 30	NSP
1: 2	1.48	13.3;26.7	Local Self-propagation (LSP)
1: 1	2.96	20; 20	LSP
2: 1	5.92	26.7;13.3	LSP
2.5:1	7.41	28.6;11.4	Full Self-propagation (FSP)
3: 1	8.89	30; 10	FSP
3.5:1	10.37	31.1;8.9	LSP
4: 1	11.85	32; 8	NSP

Footnote: Concentration: 2.0 g L^{-1}; Deposited time: 20 min; Voltage gradient: 10V/mm

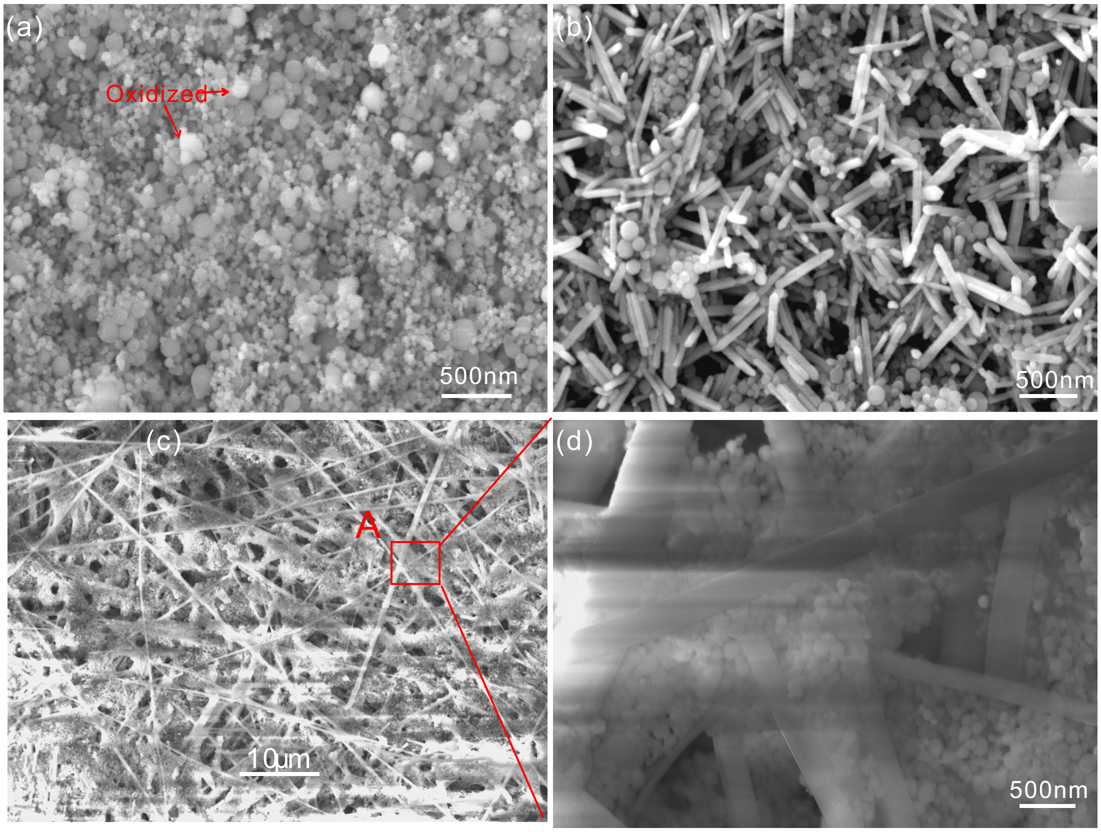

Fig. 5 SEM images of (a) Al/Fe_2O_3 (NPs) EPD film; (b) Al/Fe_2O_3 (NRs) EPD film; (c) Al/Fe_2O_3 (NWs) EPD film; (d) a large-magnified SEM image of region A in Fig. 6(c).

and instant plume speed increase as well. Note that the maximum combustion velocity (2.03 m/s) and instant plume speed (10.71 m/s) can be reached by Al/Fe_2O_3 (NPs) nanothermite with a Φ value of 7.41. However, a further increase in Φ value slows down the combustion velocity and instant plume speed of nanothermite. This reveals that Al/Fe_2O_3 (NPs) nanothermite with Φ value of 7.41 has a superior combustion performance.

Under this satisfactory Φ value (7.41), EPD samples of Al/Fe_2O_3(NRs) and Al/FeNTA (NWs) nanothermites are also prepared for comparison. Fig. 5 presents detailed SEM images of top-viewed EPD nanothermite samples. As clearly shown in Fig. 5 (a), Al and Fe_2O_3 NPs are uniformly deposited on Cu substrates with Al NPs randomly scattered around the Fe_2O_3 NPs. This reveals a homogeneously mixed film produced by the EPD method. In addition, it can be easily distinguished from the uniform matrix material that the larger ones are Al NPs, while the much finer ones are Fe_2O_3 NPs. Fig. 5b shows the SEM image of Al/Fe_2O_3 (NRs) nanothermite also with Φ value of 7.41. It evidences that the distribution of Al NPs and Fe_2O_3 NRs is a bit non-uniform with abundant Al NPs centralizing around Fe_2O_3 NRs. In addition, its film is not as compact and dense as that of Al/Fe_2O_3 (NPs) nanothermite. This inadequate interface contact potentially affects the thermite reactivity. Fig. 5c shows the morphology of Al/FeNTA (NWs) nanothermite also with Φ value of 7.41. Apparently, the Cu carrier used as electrode are overspread with Al NPs, particularly at the intersecting position of FeNTA NWs, as shown in Fig 5d, the magnified SEM image of region A Fig. 5c. Al NPs fill in the pores between FeNTA nanowires.

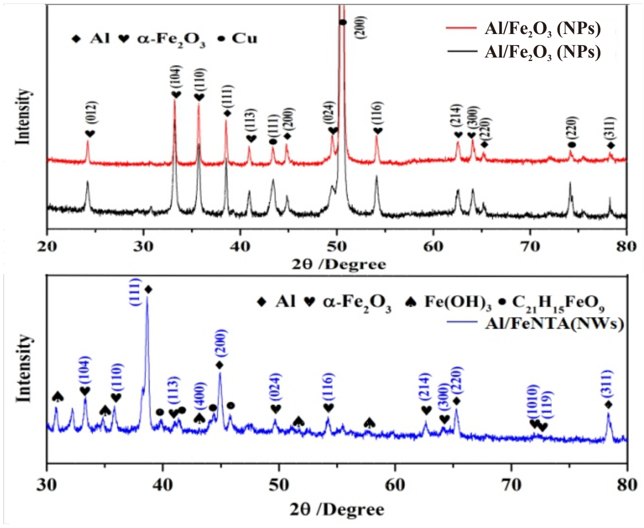

Fig. 6 XRD analysis of Al/Fe_2O_3 nanothermites EPD samples.

XRD analysis is performed to further characterize the crystal structure of EPD nanothermite samples. The results are displayed in Fig. 6. Clearly, for the XRD analyzed results of Al/Fe_2O_3(NPs) and Al/Fe_2O_3(NRs) nanothermite EPD samples, independent and relatively sharp diffraction patterns can be observed, which match well with the standard spectra for Al (JCPDS: 85-1327) and α-Fe_2O_3 (JCPDS: 33-0664). It reveals that both Al NPs and α-Fe_2O_3 NPs or α-

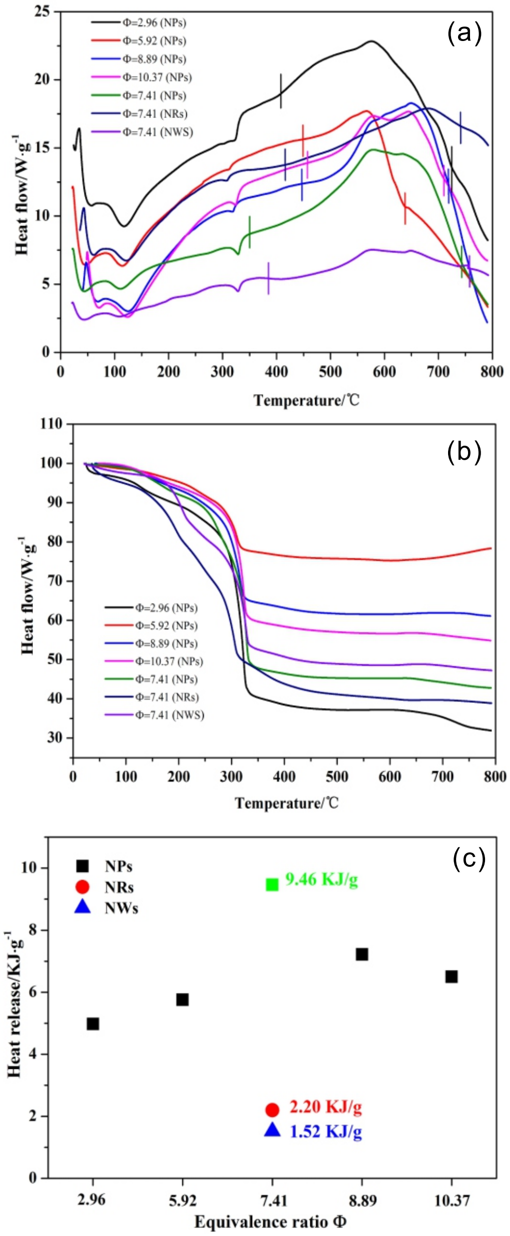

Fig. 7 The DSC (a) and TGA (b) analysis for the Al/Fe_2O_3 (NPs) nanothermite with different equivalence value Φ; (b) The dependence of the energy release per mass with the equivalence value Φ.

Fe_2O_3 NRs are successfully deposited onto the Cu substrate without any impurities. Note that the diffraction patterns of Cu phase (JCPDS: 04-0836) are originated from Cu electrode employed to deposite nanothermite. To eliminate the interference from Cu electrode, nanothermites of Al/FeNTA (NWs) are scraped from the surface of Cu electrode for XRD analysis. Corresponding results are also shown in Fig. 6. Besides the emergence of diffraction patterns of Al (JCPDS: 85-1327) and organics of $C_{21}H_{15}FeO_9$ (JCPDS: 01-0055) stemming from FeNTA, diffraction patterns of α-Fe_2O_3 (JCPDS: 33-0664) and $Fe(OH)_3$ (JCPDS: 38-0032) also can be observed. This may closely relate to the decomposition of FeNTA during hydrothermal growth, which will be further investigated in our further study.

3.3 Energy release during combustion

To evaluate the energy release from the nanothermite reaction, the heating process of the nanothermite was analyzed via DSC and TGA with temperature increasing from 25 to 800°C, as shown in Fig. 7. Clearly, for all the Al/Fe_2O_3 nanothermites, they have a small endothermic peak around 100 °C, which is consistent with a trace amount of weight loss in the TGA curve at this temperature. This probably relates to the evaporation of water. With external temperature increasing to ~350°C, another tiny endothermic peak can be observed, corresponding to a considerable amount of weight loss, as shown in the TGA curve. This is probably caused by the decomposition of organic substances. A further increase in temperature triggers the nanothermite reaction with the emergence of a broad exothermic peak at ~560°C (NPs: Φ= 2.96, 5.92, 7.41; NWs: Φ= 7.41) or at ~650℃(NPs:Φ= 8.89, 10.37; NRs: Φ= 7.41). In this case, a small amount of weight loss occurs, as obtained in the corresponding TGA curve. Worthy of note is that the DSC curve for Al/Fe_2O_3 (NPs) nanothermite with Φ value of 7.41 shows a small drop at ~610℃ in the exothermic process. This temperature is close to the melting point of bulk Al (660°C). So, this drop behavior may be explained as the melting of Al NPs in the nanothermite caused by excessive amount of Al NPs in the nanothermite. The molten Al may continue to react with Fe_2O_3 NPs and thus reaching another heat release peak. This phenomenon can also be seen from the heat release during the Al/FeNTA(NWs) nanothermite reaction. The heat output was calculated by integrating the heat flow of exothermic peak with respect to time. Corresponding results were shown in Fig. 7c. Clearly, Al/Fe_2O_3 (NPs) nanothermite with Φ value of 7.41 has the largest heat output, around 9.46 KJ/g, much larger than that produce from the nanothermite reactions of Al/Fe_2O_3 (NRs) and

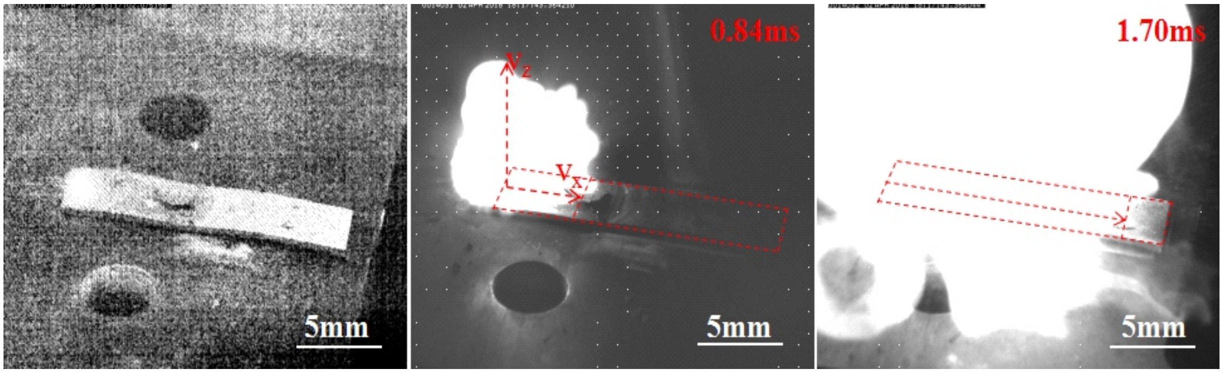

Fig. 8 A series of flame propagation images for the Al/Fe_2O_3 (NPs) nanothermite with the optimal equivalence value Φ of 7.41.

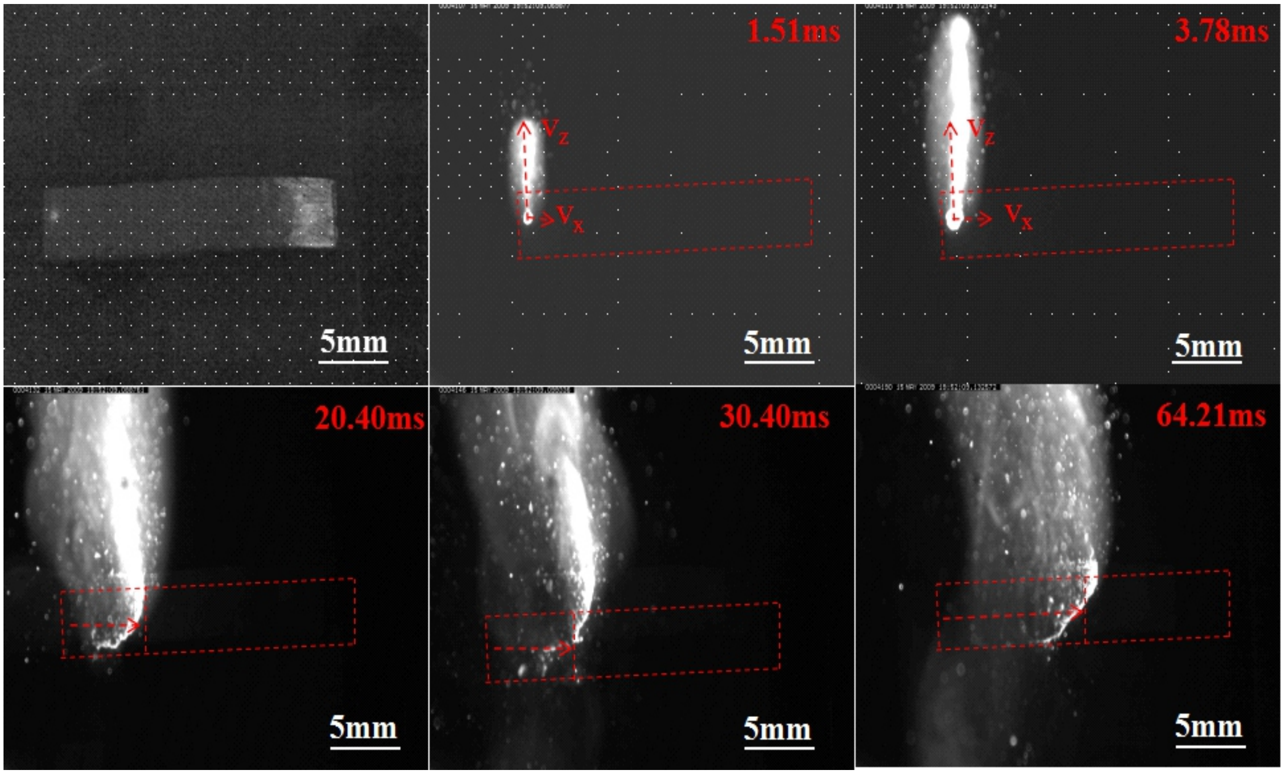

Fig. 9 A series of flame propagation images for the Al/Fe_2O_3 (NRs) nanothermite with Φ value of 7.41.

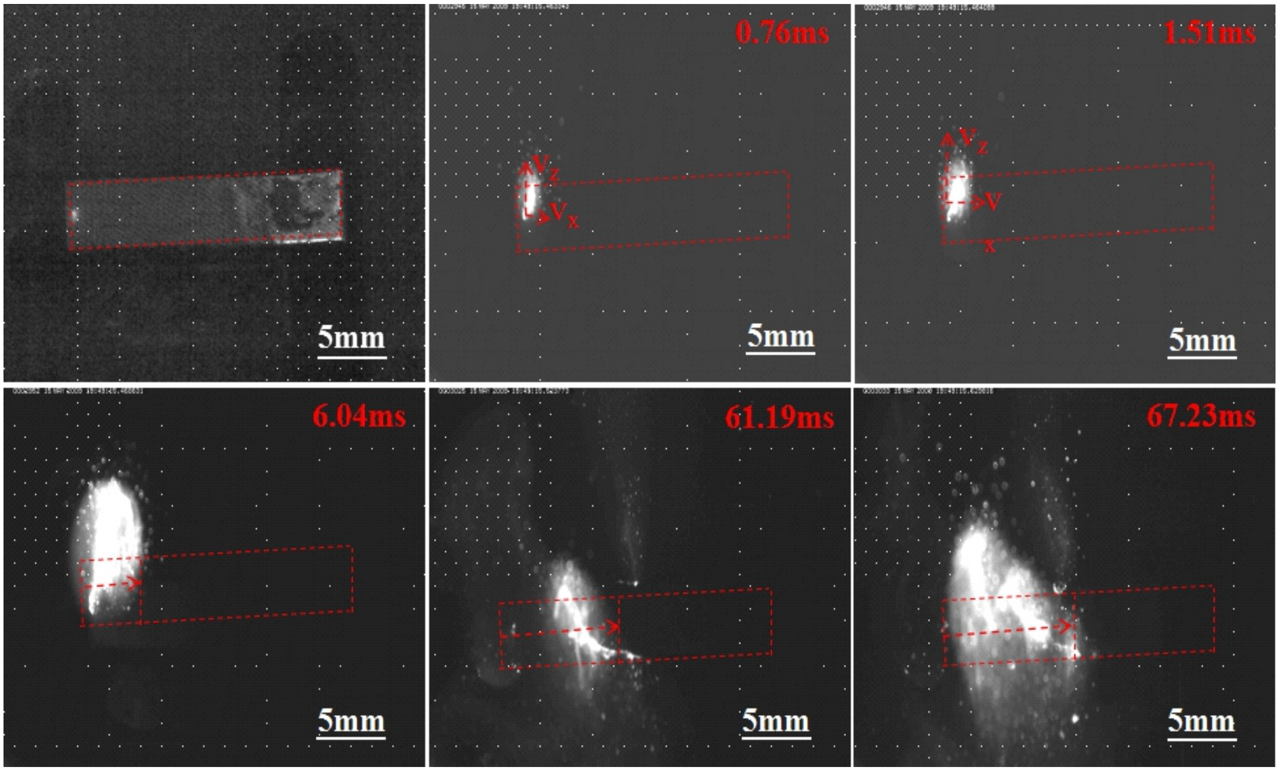

Fig. 10 A series of flame propagation images for the Al/FeNTA (NWs) nanothermite with Φ value of 7.41.

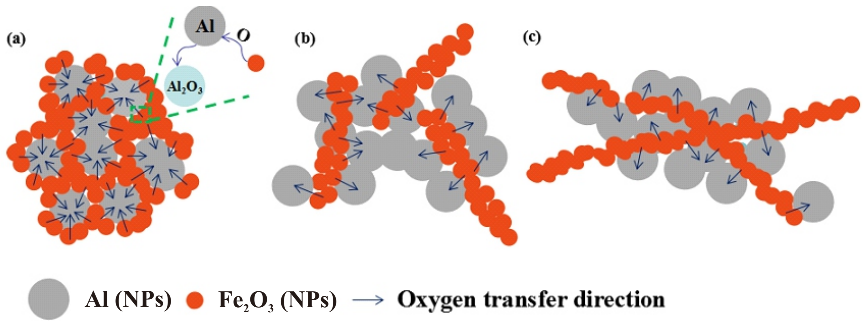

Fig. 11 Schematic illustration of nanothermite reactions of (a) Al/Fe_2O_3 (NPs), (b) Al/Fe_2O_3 (NRs) and (c) Al/FeNTA (NWs).

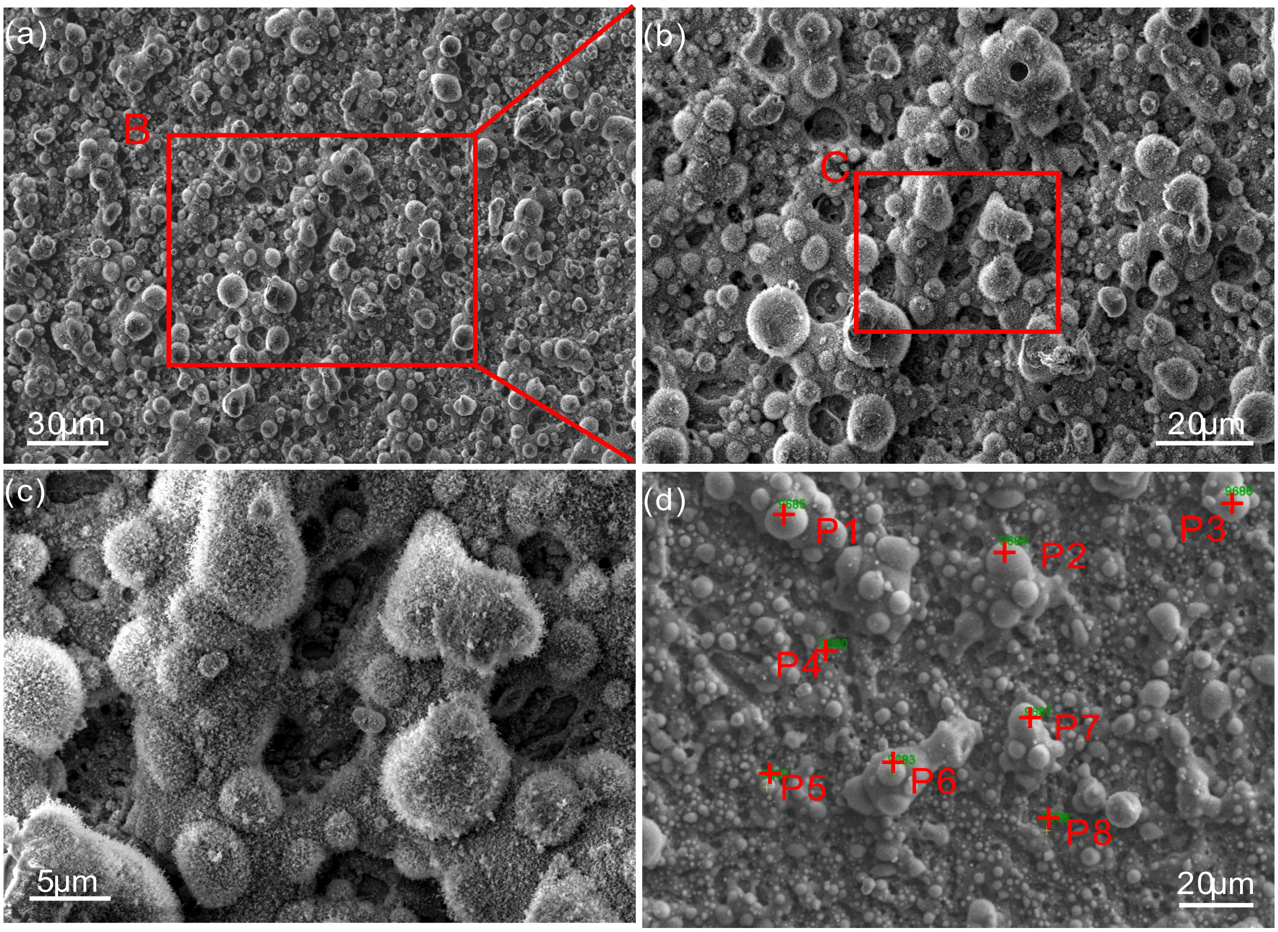

Fig. 12 (a) SEM image of products formed in the Al/Fe_2O_3 (NPs) nanothermite reaction; (b) a low-magnified SEM image of region B in Fig. 12(a); (c) a large-magnified SEM image of region C in Fig. 12(b); (d) SEM image of the products from the Al/Fe_2O_3 (NPs) nanothermite reaction for EDS analysis.

Al/Fe_2O_3 (NWs) with the same Φ value (7.41). Ref. [29] reported that the total heat release of Al/Fe_2O_3 micro-thermite only reaches 0.2 KJ/g. Ke et al.[17] once successfully deposited Al/Fe_2O_3 nanothermite on Cu electrode and its heat release can approach 1.85 kJ/g. Here, the particle size of Al NPs and Fe_2O_3 NPs are decreased to be 90 nm and 40 nm, respectively. They are about 1.5-2 times larger than the nanothermite used in this study. Hence, it can be concluded the amount of heat release during thermite reaction closely relates to the size of fuels (Al) and oxidizers (Fe_2O_3) due to the difference in interface contact distance between Al and Fe_2O_3 NPs.

In Section 3.2, a preliminary exploration of the relationship between the combustion velocity of Al/Fe_2O_3 (NPs) nanothermite and the equivalence ratio Φ has been conducted, as expressed in Fig. 4. We have already obtained that as Φ value increases to 7.41, both the combustion velocity and the instant plume speed can reach the maximum, around 2.04m/s and 10.71m/s, respectively. The combustion was recorded using a high-speed camera, as shown in Fig. 8. Apparently, Al/Fe_2O_3 (NPs) nanothermite reaction (Φ=7.41) produces glaring ashes and bright sparkling, indicative of a full reaction with a considerable heat release.

By comparison, a series of combustion frames of Al/Fe_2O_3 (NRs) and Al/FeNTA (NWs) nanothermites (Φ=7.41) are also given in Fig. 9 and Fig. 10, respectively. Clearly, the combustion reactions of both Al/Fe_2O_3 (NPs) and Al/FeNTA (NWs) nanothermite are much slower with milder sparkling. The combustion velocity and instant plume speed are calculated to be 0.16m/s and 4.96 m/s, and 0.098 m/s and 3.28m/s, respectively. It strongly demonstrates that both the heat release and the combustion velocity during the nanothermite reaction are highly correlated with the shape of nano-Fe_2O_3 oxidizers. Fe_2O_3 oxidizers with spherical shape induce a much stronger combustion than another two shapes.

In fact, the thermite reaction (R. 2) is a process where oxygen transfers from metal-oxide to another metal which will be oxidized. Hence, the oxygen transfer dynamics can considerably influence the combustion velocity of thermite reaction.[30] Fig. 11 gives the schematic illustration of the oxygen transfer during these three kinds of nanothermite reactions. Note that the illustration of the distribution of Al NPs and Fe_2O_3 with various shapes is based on the morphology observation results in Section 3.2. For Al/Fe_2O_3 nanothermite, Al NPs and Fe_2O_3 NPs are mixed relatively uniformly, so that oxygen transferring from Fe_2O_3 nano-oxidizer to Al NPs becomes much easier. This is attributed to the shape advantage of spherical Fe_2O_3 NPs, making the oxygen between Fe_2O_3 NPs and Al NPs isotropically, as illustrated in Fig. 11a. However, for Al/Fe_2O_3 (NRs) or Al/FeNTA (NWs) nanothermite, Al NPs are prone to distribute along the outside edge of Fe_2O_3 NRs or FeNTA (NWs), creating the anisotropic oxygen transfers mainly pointing to the interfaces. The inhomogeneous distribution of oxygen brought by the shape shortcoming leads to an inadequate nanothermite reaction. Hence, in comparison with the Al/Fe_2O_3 (NRs) and Al/FeNTA (NWs) nanothermites, Al/Fe_2O_3 (NPs) nanothermite reaction exhibits a distinctly increased combustion speed with much more released heat.

3.4 Microstructure characterization of reaction products

Fig. 12 shows the SEM images of products from the Al/Fe_2O_3 (NPs) nanothermite reaction. From Fig. 12a&b, it is clear that most products distributed on a porous matrix retain their original sphere morphology with a micro-size. Obviously, reactive sintering of NPs also occurs during the reaction. It is conducive to improving the combustion reaction since sintering contributes to more intimate interface contact between these NPs. With a high magnification, villiform nanofibers can be observed to emerge on the surfaces of these spheroidal products after the combustion, indicating the fast growth of whiskers Fig. 12c. To have a complete understanding of the compositions of these products, several points in Fig. 12d were selected to be analyzed by EDS, the results of which are listed in Table 2. It can be seen only for Point P4 and P8, representing porous matrix, elemental O has a higher atom percent than elemental Al and their atom ratio is close to 1.5, revealing the porous matrix is in fact the newly formed Al_2O_3. Note that P8 has a relatively high Cu atom percent, probably caused by the Cu substrate serving as an electrode to deposit nanothermite. Besides P4 and P8, it is hard to have a

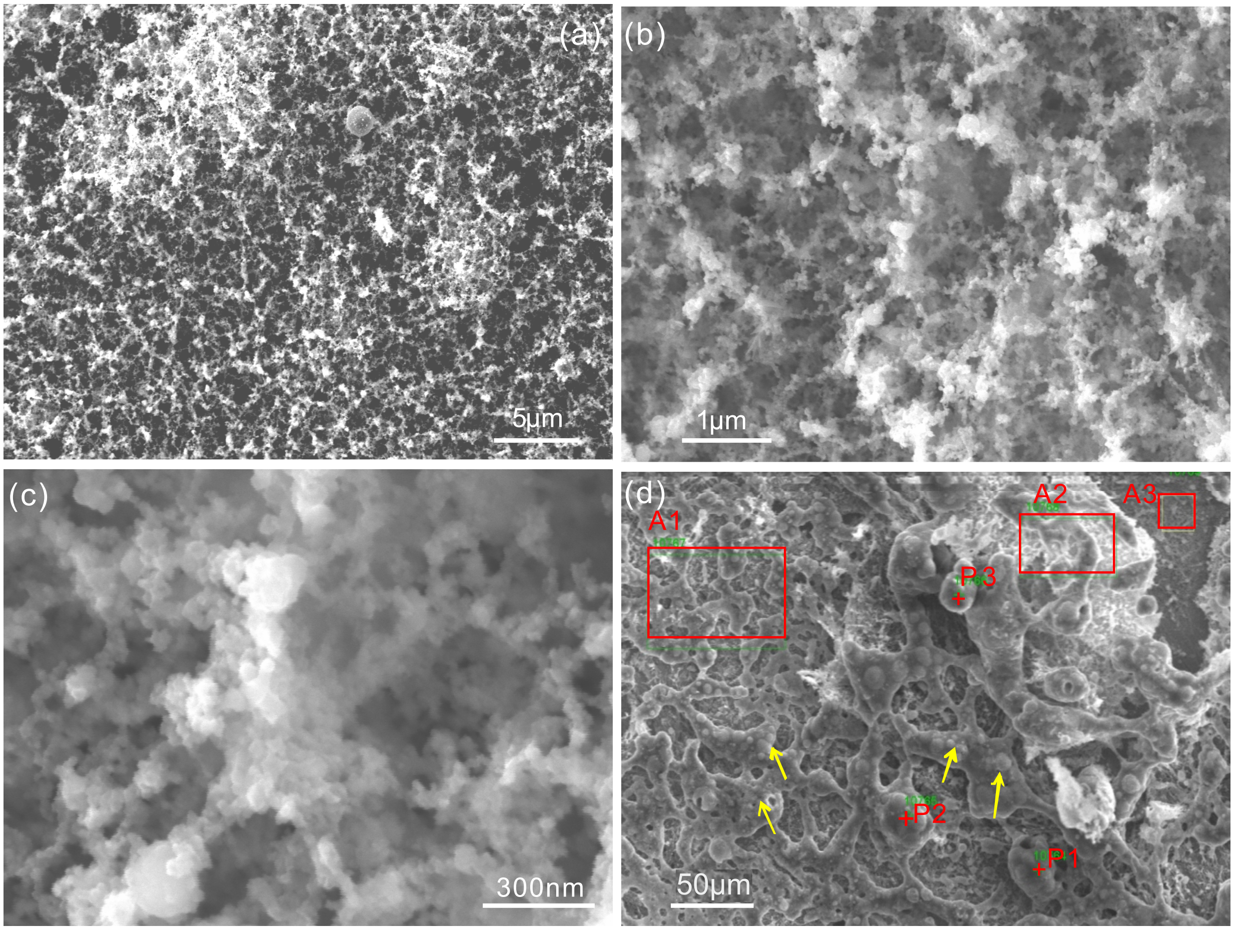

Fig. 13 SEM image of products formed in the Al/Fe_2O_3 (NRs) nanothermite reaction.

Table 2. EDS analyzed results of products formed in the Al/Fe2O3 (NPs) nanothermite reaction.

Element position	O (wt.%/At.%)	Al (wt.%/At.%)	Fe (wt.%/At.%)	Cu (wt.%/At.%)
Point 1	17.87/30.25	58.06/58.08	23.95/11.62	0.12/0.05
Point 2	26.40/39.76	58.42/52.05	14.67/6.27	0.51/1.92
Point 3	24.42/37.5	62.64/56.86	12.94/5.64	0/0
Point 4	28.60/48.12	36.96/36.83	11.94/5.65	22.5/9.40
Point 5	23.99/40.76	43.02/43.21	32.31/15.76	0.68/0.27
Point 6	18.15/32.49	46.22/49.17	35.11/18.11	0.52/0.23
Point 7	26.2/40.32	58.03/52.86	15.34/6.64	0.43/0.18
Point 8	16.3/33.5	33.09/40.39	4.22/2.46	46.39/23.65

Table 3. EDS analyzed results of products formed in the Al/Fe2O3 (NRs) nanothermite reaction.

Element position	O (wt.%/At.%)	Al (wt.%/At.%)	Fe (wt.%/At.%)	Cu (wt.%/At.%)
Point 1	53.80/67.09	42.87/31.75	2.88/1.02	0.44/0.14
Point 2	13.00/23.65	55.74/60.15	29.66/15.47	1.60/0.73
Point 3	39.82/57.32	41.12/34.99	17.52/7.14	1.54/0.55
Area 1	27.71/43.36	51.98/48.37	8.54/3.76	11.76/4.51
Area 2	34.14/48.85	55.02/46.79	7.61/3.21	3.23/1.15
Area 3	27.05/46.43	36.90/37.64	8.01/3.85	28.05/12.08

Table 4. EDS analyzed results of products formed in the Al/FeNTA (NWs) nanothermite reaction.

Element position	O (wt.%/ At.%)	Al (wt.%/ At.%)	Fe (wt.%/ At.%)	Cu (wt.%/ At.%)
Area 1	35.21 /52.38	45.18 /39.76	11.91 /5.06	7.70 /2.8
Area 2	35.11/55.03	35.41/32.91	9.55/4.27	19.93/7.79
Area 3	25.98/55.03	1.29/1.62	71.27/43.14	1.46/0.21

certain judgement of other analyzed points taken from the micro-scale particles because of their atypical atom ratios, which are required to be further analyzed through XRD technique.

Fig. 13 gives the SEM images of products created in the Al/Fe_2O_3(NRs) combustion process. As shown in Fig. 13a, it is clear that after reaction, a loose and porous reaction surface emerges with few micro-scaled sintered particles distributing on it. A further magnified SEM image of this surface morphology in Fig. 13b and (c) present that these porous structures are in fact composed of numerous NPs Fig. 13c. Again, it is clear from Fig. 13d that a sintered and melted behavior can be observed due to the emergence of river-patterned metal or IMC band with some sintered NPs lying in it (marked with yellow arrow). Table 3 summarized the EDS analyzed results for some points or regions. It can be seen the atom ratio of O to Al for P1 and P3 is close to 1.5~2 and Cu has a much lower atom percent. It can probably be inferred that these two micro-sized particles are Al_2O_3. For P2, the atom ratio between Fe and O approaches 1.5, revealing the formation of Fe_3O_4. However, the content of elemental Al is also very high here, which required further XRD phase analysis. For Area A1 and A2, it is also hard to accurately judge the detail phase due to their similar content of elemental O and Al. However, the products on A3 can be determined as Al_2O_3 according to their atom ratio.

For the Al/FeNTA (NWs) nanothermite reaction, corresponding SEM image for the products are presented in Fig. 14. Obviously, the original wire shape is somewhat retained after combustion reaction Fig. 14a. Interestingly, with a gradual magnification of these reacted wires, it is clear that they are composed of numerous sintered NPs Fig. 14d. After a basic EDS analysis of this area (A1, Table 4), it can be judged that they are Al_2O_3 based on its Al/O atom ratio. Besides,

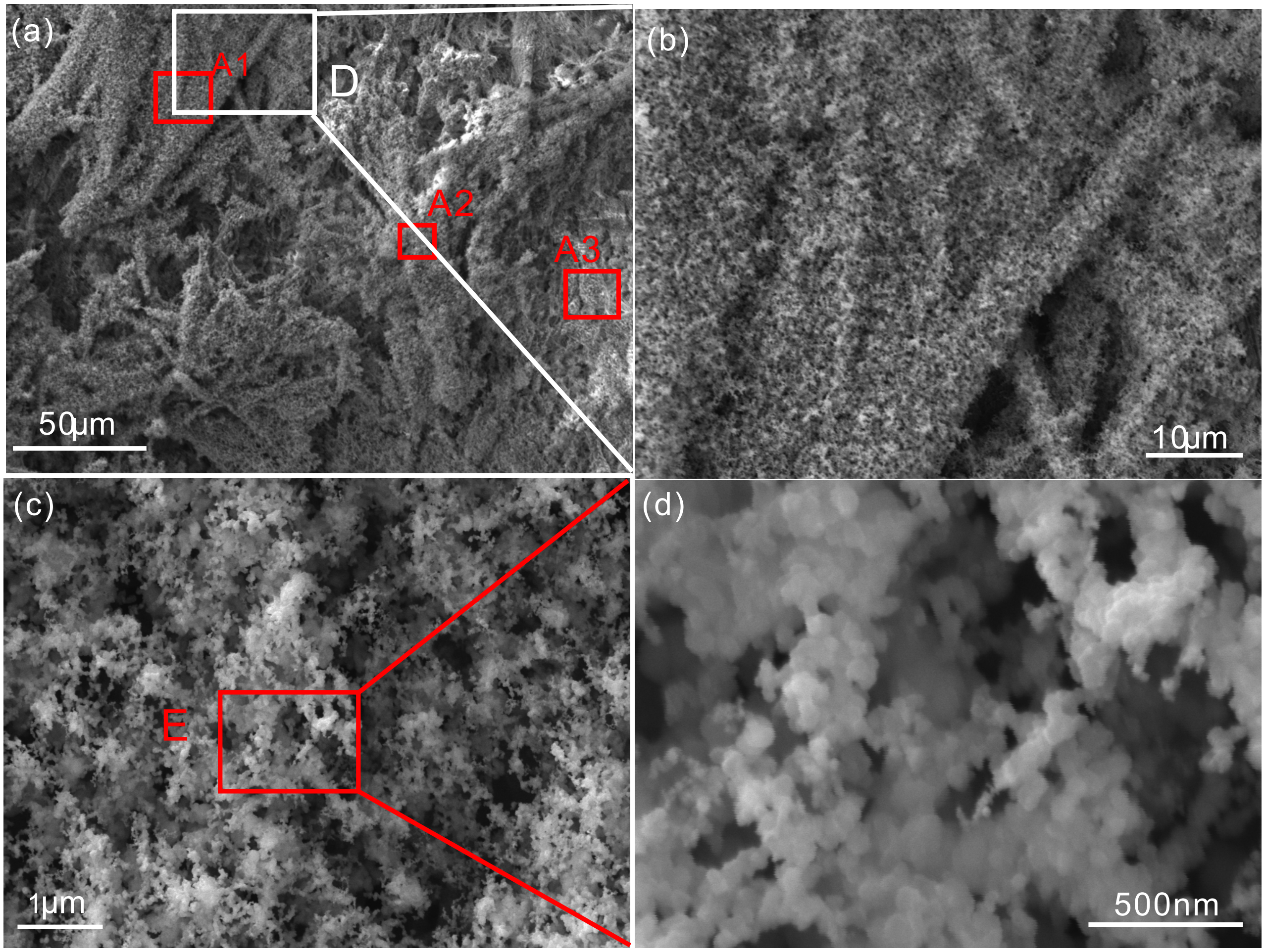

Fig. 14 (a) SEM image of products formed in the Al/FeNTA (NWs) nanothermite reaction; (b) a low-magnified SEM image of region D in Fig. 14(a); (c) a large-magnified SEM image of one region in Fig. 14(b); (d) a more large magnified SEM image of region E in Fig. 14(c).

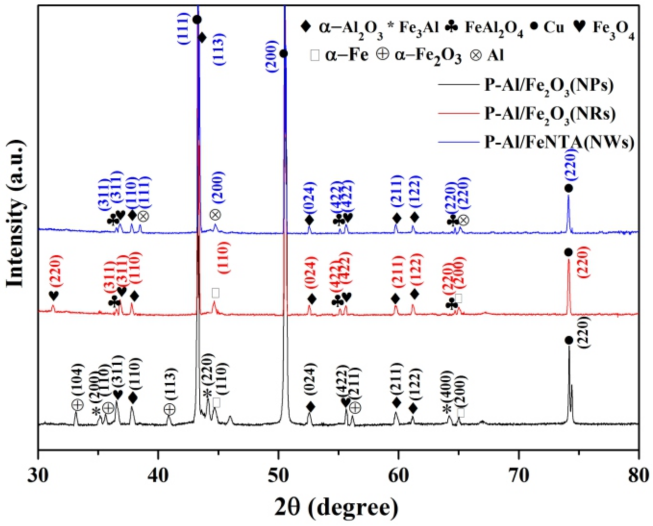

Fig. 15 XRD analysis of products formed in the Al/Fe_2O_3 nanothermite reactions.

for A2, the same results can be obtained. However, for A3, the content of Al is decreased and the atom ratio between elemental O and Fe is close to 1.3, indicative of the formation of Fe_3O_4, which need to be further analyzed by XRD measurement.

To identify phases formed in the nano-thermite reaction (Φ=7.41) through SEM, XRD measurement was performed then, the results of which are present in Fig. 15. It is clear that for these three kinds of nanothermite reactions, α-Al_2O_3 phase (JCPDS: 10-0173) emerge in all of their reaction products. In addition, the diffraction peaks of α-Fe phase (JCPDS: 06-0696) also appear in the reaction products of Al/Fe_2O_3(NPs) and Al/Fe_2O_3 (NRs) nanothermite. Accordingly, the occurrence of nanothermite reaction (R. 2) is supposed to occur. However, the absence of α-Fe phase in the reaction products of Al/FeNTA (NWs) nanothermite is probably due to its small amount that cannot be detected by the XRD technique. Note that intermediate product of Fe_3Al was found to exist in the reaction products of Al/Fe_2O_3 (NPs) nanothermite, while that of $FeAl_2O_4$ was produced during the nanothermite reaction of Al/ Fe_2O_3 (NRs) and Al/FeNTA (NWs). Their emergence is probably based on the following reactions:[31,32]

$$3Fe_2O_3 + 8Al \rightarrow 2Fe_3Al + 3Al_2O_3 \quad (3)$$

$$3Fe_2O_3 + 2Al \rightarrow 5FeO + FeAl_2O_4 \quad (4)$$

It is hard to monitor the actual reaction temperature of the above intermediate reactions (R. 3 and R. 4). These kinds of intermediate products like AlNi, Cu_2O were also reported to emerge during the Al/NiO and Al/CuO nanothermite reaction.[1,18,33] Generally, these intermediate products were produced at a relatively low reaction temperature since these reactions are intermediate processes. In addition, the diffraction peaks of Fe_3O_4 phase with a low intensity were also observed to emerge during these three kinds of nanothermite reactions. The fabrication method for Fe_3O_4 IMCs in different nanothermite reactions is supposed to be different, which depends on the actual temperature reached by the respective nanothermite reaction. However, based on the difference in heat release, it can be initially concluded that the emergence of Fe_3O_4 IMCs in the Al/Fe_2O_3 (NPs) nanothermite reaction is probably due to the decomposition of Fe_2O_3 at a relatively high temperature (~1500°C), while those appearing in the Al/Fe_2O_3(NRs) or Al/FeNTA (NWs) nanothermite reaction are possibly due to the oxidation of unstable FeO at about 500°C. Here FeO is formed along with the production of $FeAl_2O_4$ (R. 4).

To know the actual reaction steps for each nanothermite reaction, more work should be done on monitoring the reaction temperature and employing more accurate techniques to detect and identify the intermediate and final reaction products. For the potential application, these nanothermite reactions can also be deposited onto a conductive electrode on a Polyimide (PI) using EPD method to fabricate deflection sensors due to the advantages of their specific shape and self-sintering advantage.[34,35]

4. Conclusion

In this study, α-Fe_2O_3 oxidizers with different shapes (NPs, NRs and NWs) have been successfully fabricated. As the nominal weight ratio of Al/Fe_2O_3 (NPs) approaches 2.5:1, the average combustion velocity and the instant plume speed of the Al/Fe_2O_3 (NPs) nanothermite reaction can reach the maximum, around 2.04 and 10.71 m/s, respectively. In this case, the heat release also reaches the largest, ~9.46 KJ/g. However, under the same nominal weight ratio, the average combustion velocity and the instant plume speed of both Al/Fe_2O_3 (NRs) and Al/FeNTA (NWs) nanothermites are only about 0.16m/s and 4.96 m/s, and 0.098 m/s and 3.28m/s, respectively. This is probably due to the shape difference that renders different contact distance between nano-fuel and nano-oxidizer. In the future work, the weight ratio for Al/Fe_2O_3 (NRs) and Al/FeNTA (NWs) nanothermite can be further adjusted to find their respective optimal reaction ratio and achieve superior combustion performance. In addition, directly igniting Al/FeNTA nanothermite seems not a good strategy. So, to tailor it, a previous calcination of FeNTA precursor NWs is suggested to make them completely convert to Fe_2O_3 NWs, so that they can react with Al NPs more fully. In addition, these nanothermite reactions can also be deposited onto a conductive electrode on a Polyimide (PI) using EPD method to fabricate deflection sensors due to the advantages of their unique microstructure and self-sintering features.

Acknowledgement

This project is partially supported by the Mission Seed Grant of UT Research office and Engagement, National Natural Science Foundation of China (Grant No. 51675269, 51575016) and the Priority Academic Program Development of Jiangsu Higher Education Institutions (PAPD).

References

1. J. Wang, A. M. Hu, J. Persic, J. Z. Wen, Y. N. Zhou, *J. Phys. Chem. Solids*, 2010, **72**, 620-625.
2. D. X. Zhang, X. M. Li, B. Qin, C. Lai, X. G. Guo, *Mater. Lett.*, 2014, **120**, 224-227.
3. H. Sui, S. Atashin, J. Z. Wen, *Thermochim. Acta*, 2016, **642**, 17-24.
4. C. W. Farley, M. L. Pantoya, V. I. Levitas, *Combust. Flame*, 2014, **161**, 1131-1134.
5. J. Sun, M. L. Pantoya, S. L. Simon, *Thermochim. Acta*, 2006, **444**, 117-127.
6. Y. Ma, H. Li, D. Bridges, P. Peng, B. Lawrie, Z. L. Feng, A. M. Hu, *RSC. ADV.*, 2016, **6**, 75916-75936.
7. K. S. Martirosyan, *J. Mater. Chem.*, 2011, **21**, 9400-9405.
8. N. H. Yen, L. Y. Wang, *Explos., Pyrotech.*, 2012, **37**, 143-155.
9. J. Shen, Z. Qiao, J. Wang, K. Zhang, R. Li, F. Nie, G. Yang, *Combust. Flame*, 2014, **161**, 2975-2981.
10. V. E. Sanders, B. W. Asay, T. J. Foley, B. C. Tappan, A. N. Pacheco, S. F. Son, *J. Propul. Power*, 2007, **23**, 707-714.
11. M. L. Pantoya, V. I. Levitas, J. J. Granier, J. B. Henderson, *J. Propul. Power*, 2009, **25**, 465-470.
12. K. T. Sullivan, M. A. Worsley, J. D. Kuntz, A. E. Gash, *Combust. Flame*, 2012, **159**, 2210-2218.
13. S. H. Kim, M. R. Zachariah, *Adv. Mater.*, 2004, **16**, 1821-1825.
14. Y. Ohkura, S. Y. Liu, P. M. Rao, X. L. Zheng, *P. Combust. Inst.*, 2011, **33**, 1909-1915.
15. J. Y. Malchi, T. J. Foley, R. A. Yetter, *ACS. Appl. Mater. Interfaces*, 2009, **1**, 2420-2423.
16. K. B. Plantier, M. L. Pantoya, A. E. Gash, *Combust. Flame*, 2005, **140**, 299-309.
17. X. Ke, X. Zhou, H. Gao, G. Hao, L. Xiao, T. Chen, J. Liu, W. Jian, *Mater. Des.* 2017, **140**, 179-187.
18. J. Z. Wen, S. Ringuette, G. Bohloulizanjani, A. M. Hu, N. H. Nguyen, J. Persic, C. F. Petre, Y. N. Zhou, *Nano Res. Lett.*, 2013, **8**, 184-184.
19. R. Shende, S. Subramanian, S. Hasan, S. Apperson, R. Thiruvengadathan, K. Gangopadhyay, S. Gangopadhyay, P. Redner, D. Kapoor, S. Nicolich, W. Balas, *Propellants Explos. Pyrotech.*, 2008, **33,** 122-130.
20. B. Siegert, M. Comet, O. Muller, G. Pourroy, D. Spitzer, *J. Phys. Chem. C*, 2010, **114**, 19562-19568.
21. J. T. Zhang, J. F. Liu, Q. Peng, X. Wang, Y. D. Li, *Chem. Mater.*, 2006, **18**, 867-871.
22. Y. Ji, W. Kim, K. Cho, D. Lee, S. H. Kim, *Powder Tech.*, 2011, **211**, 65-71.
23. L. J. Qin, N. Yan, J. G. Li, H. X. Hao, F. Q. Zhao, H. Feng, *RSC ADV.*, 2017, **7**, 7188-7197.
24. W. Zhang, B.Yin, R. Shen, J. H. Ye, J. A. Thomas, Y. M. Cha, *Appl. Mater. Interfaces*, 2013, **5**, 239-242.
25. Y. C. Yu, M. Chen, S. T. Wang, C. Hill, P. Joshi, T. Kuruganti, A. M. Hu, *J. Electrochem. Soc.*, 2018, **165**, A584-A592.
26. G. H. Qiu, H. Huang, H. Genuino, N. Opembe, L. Stafford, S. Dharmarathna, S. L. Suib, *J. Phys. Chem. C*, 2011, **115**, 19626-19631.
27. Z. Li, X. Lai, H. Wang, D. Mao, C. J. Xing, D. Wang, *Nanotech.*,

2009, **20**, 245603.

28. G. X. Wang, X. L. Gou, J. Horvat, J. Park, *J. Phys. Chem. C*, 2008, **112**, 15220-15225.
29. R. H. Fan, H. L. Lv, K. N. Sun, W. X. Wang, X. B. Yi, *Thermochim. Acta*, 2006, **440**, 129-131.
30. Y. Dong, D. Yan, J. He, X. Li, W. Feng, H. Liu, *Surf. Coat. Tech.*, 2004, **179**, 223-228.
31. L. Durães, B. F. O. Costa, R. Santos, A. Correia, J. Campos, *A. Portugal, Mater. Sci. Eng. A*, 2007, **465**, 199-210.
32. J. Mei, R. D. Halldearn, P. Xiao, *Scripta. Mater.*, 1999, **41**, 541-548.
33. G. Bohlouli-Zanjani, J. Z. Wen, A. M. Hu, J. Persic, S. Ringuette, Y. N. Zhou, *Thermochim. acta*, 2013, **572**, 51-58.
34. A. M. Hu, J. Y. Guo, H. Alarifi, G. Patane, Y. Zhou, G. Compagnini, and C. X. Xu, *Appl. Phys. Lett.*, 2010, **97**, 153117.
35. P. Peng, A. M. Hu, A. P. Gerlich, G. Zou, L. Liu, Y. N. Zhou, *Acs Appl. Mater Interfaces*, 2015, **7**, 12597-12618.